Arabian Journal of Chemistry (2021) **14**, 103113

King Saud University

**Arabian Journal of Chemistry**

www.ksu.edu.sa
www.sciencedirect.com

ORIGINAL ARTICLE

# Solid-state synthesis of nitrogen-doped graphitic nanotubes with outstanding electrochemical properties

**Muhammad Rashad** [a], **Muhammad Asif** [b,*]

[a] *School of Materials Science and Engineering, Jiangsu University of Science and Technology, Zhenjiang 212003, Jiangsu, China*
[b] *Department of Chemical Sciences, University of Limerick, Limerick V94 T9PX, Ireland*

Received 24 December 2020; accepted 28 February 2021
Available online 17 March 2021

**KEYWORDS**

Potassium-ion battery;
Nitrogen-doped graphitic nanotubes;
Electrochemical Characterizations;
Energy Storage

**Abstract** Synthesis of new anodes is crucial for commercialization of rechargeable potassium-ion batteries (PIBs). In this work, the nitrogen-doped graphitic nanotubes (NGTs) were synthesized by solid-state reaction method. The microstructural characterization of synthesized NGTs revealed the presence of many active sites (provided by N-doping i.e. $N_p$ and $N_g$) and tubular channels for the $K^+$ ion transport. The NGTs electrode was tested against potassium metal in the presence of carbonate based electrolytes. The NGTs revealed the maximum reversible capacity of 220 mA h $g^{-1}$ at 20 mA $g^{-1}$ current density. Furthermore, the cycle stability of NGTs was confirmed by cycling it for 200 times at the current density of 100 mA $g^{-1}$, where specific capacity of 81.2 mA h $g^{-1}$ was retained. The excellent electrochemical properties (rate capability) and fast synthesis of NGTs highlights its possibility to be used against post-lithium metal anodes in near future.


## 1. Introduction

Potassium ion battery (PIBs) has arisen as a new kind of metal ion battery with several advantages such as high potassium reservoirs on earth crust (making PIBs cheaper) and redox potential of potassium is almost equal to that of lithium verses SHE (−2.93 V ≈ −3.05 V) (Kim et al., 2018). Despite of these fabulous advantages, PIBs are restricted owing to the large atomic radius of potassium ions (2.66 Å), which causes the sluggish potassium ion transportation during redox reactions (Shannon, 1976). Furthermore, it is well known that during redox reactions, host materials endures from structural breakdowns owing to insertion and extraction of guest ions, ultimately leading to the poor cycle stabilities of resultant PIBs (Xue et al., 2017; Zhang et al., 2017). Thus, to overcome these problems, synthesis of highly stable host materials is extremely needed. Literature review revealed that carbon-based electrode materials have been widely explored to maintain the cycle performance of PIBs (Jian et al., 2015; Luo et al., 2015; Cohn et al., 2016; Share et al., 2016; Xu et al., 2018). However, most of the synthesized carbon structures exhibited low electrochemical performance and working potentials (Jian et al.,

* Corresponding author.
E-mail address: Muhammad.asif@ul.ie (M. Asif).
Peer review under responsibility of King Saud University.

ELSEVIER Production and hosting by Elsevier

https://doi.org/10.1016/j.arabjc.2021.103113
1878-5352 

2015; Luo et al., 2015). Besides carbon structures, the development of transition metal oxides such as $K_2Ti_8O_{17}$ (Han et al., 2016b), $K_2Ti_4O_9$ (Kishore et al., 2016), $KTi_2(PO_4)_3$ (Han et al., 2016a), and $TiO_xN_x$/C (Tao et al., 2019) etc. was also carried out to achieve the high specific capacity and working potential for PIBs. Although, these metal oxides exhibit small volume expansion during charging and discharging process, however low specific capacity (i.e. 130 mA h $g^{-1}$) was attained, mainly due to the poor electrical conductivity of host material (Daigle et al., 2019).

Recently, several other materials were also explored to store the potassium ions. For example, the nano-porous germanium (NPGe) synthesized by Yang et al. (Yang et al., 2019) was employed as cathode materials against K metal anode. The NPGe-based PIB revealed the reversible capacity of 120 mA h $g^{-1}$ at 20 mA $g^{-1}$. Similarly, the potato-derived activated porous carbon displayed the capacity of 248 mA h $g^{-1}$ at 100 mA $g^{-1}$ with excellent cycle stability (Cao et al., 2019). Furthermore, vanadium oxide ($V_2O_5$) – reduced graphene oxide nanocomposites, tin oxide nanostructures, and para-disodium-2, 5-dihydroxy-1,4-benzoquinone (p-$Na_2C_6H_2O_6$) were also investigated for PIBs (Chen and Zhao, 2019; Suo et al., 2019; Vishnuprakash et al., 2019). Unfortunately, these materials exhibited poor electrochemical properties (i.e. rate performance, cycle performance etc.) for PIBs.

Besides transition metal oxides, the synthesis of metallic nano particles (i.e. Si, Sb, etc.) and their use as anode material in different kind of rechargeable batteries have also been explored recently (Singh et al., 2013; Li et al., 2014; Obrovac and Chevrier, 2014; Wang et al., 2018). These metallic nano particles support the redox process through alloying reactions (Gong et al., 2016; Ji et al., 2017). Unfortunately, the main hurdle of these materials is their cluster formations, which may lead to low electrochemical capabilities (Zhang et al., 2018a). Therefore, the exploration of new host materials with sufficient working potentials, high electrical conductivities and specific capacities, are highly required to develop the PIBs. Inspired from the electrical conductivity and theoretical capacity of carbon nanostructures, here in nitrogen-doped graphitic nanotubes (NGTs) are synthesized using solid-state reaction route. The NGTs cathode exhibited excellent rate performance (220 mA h $g^{-1}$ at 20 mA $g^{-1}$) and cycle stability (81.2 mA h $g^{-1}$) against potassium metal anode in carbonate based electrolytes.

## 2. Experimental section

### 2.1. Synthesis

All chemicals were used without further purification. Typically, the 2.5 g of polyethylene glycol, PEG-6000 (0.4167 mM, Adamas, 99%) and urea (27.5 g, Sigma-Aldrich, 99.88%) were mixed in 500 ml deionized water using magnetic stirrer at room temperature. Later, the water was removed from the mixture at 80° C and obtained composite mixture was grounded before heat treatment. The grounded composite mixture was placed in a ceramic boat and treated at 900° C for 4 h in the presence of argon atmosphere. The ramp rate was set at 5° C / min. The furnace was naturally cool down to obtain the nitrogen-doped graphitic nanotubes (GNTs). The total yield after heat treatment was about 100 mg and method is simple, which can be easily scaled up.

### 2.2. Materials characterizations

As synthesized NGTs powder was examined by X-ray photoelectron spectroscopy (XPS) and X-ray diffraction (XRD) technique in the 2$\theta$ range of 15–60°. Brunauer-Emmett-Teller (BET) technique was used to obtain the nitrogen adsorption and desorption isotherms for specific surface area measurements of NGTs (Fagerlund, 1973). Raman spectroscopy was carried out using a Renishawin Via plus operated at 632.8 nm with He-Ne laser and laser power of 4.0 mW. The surface morphology of NGTs was examined using Scanning Electron Microscopy (FESEM, JEOL, JSM-7800F) and Transmission Electron Microscopy (TEM, JEOL, JEM-2100).

### 2.3. Electrochemical characterizations

Synthesis of electrodes was carried out using doctor blade method. Firstly, the composite slurry was made by mixing the 70 wt% of NGTs, 20 wt% of Super P, and 10 wt% of polyvinylidene fluoride binder in the presence of N-Methyl-2-pyrrolidone. After blending for 4 h, the slurry was casted onto a graphite foil using doctor blade method (Asif et al., 2018) and dried in an electric oven. The foil was punched into 10 mm diameter discs and loading of active materials was about 0.9 mg.$cm^{-2}$. Half-cells were assembled in argon filled glove box using NGTs as positive electrode, potassium metal disc (16 mm diameter) as reference and counter electrode, Whatman microfiber glass as separators, and 0.8 M $KPF_6$ – diethyl carbonate (DEC) / ethylene carbonate (EC) (V/V: 1/1) as an electrolyte. The assembled cells were kept at room temperature for 5 h before testing. Cyclic voltammetry (CV) test was conducted using a potential rage of 0.9–3.3 V at different scan rate (0.1, 0.2, 0.5, 1.0, 2.0 mV $s^{-1}$). LAND battery testing station (LANHE, Wuhan) was used to test the galvanostatic charging and discharging curves in terms of rate and cycle performances. The impedance test (Nyquist plots) was conducted using an electrochemical station between 0.01–$10^6$ Hz at room temperature.

## 3. Results and discussion

In-situ synthesis of nitrogen-doped graphitic nanotubes (NGTs) is shown in Fig. 1**a**. When mixture powder was heated at 900° C, the pyrolysis of polyethylene glycol occurs to form the graphitic nanotubes. The presence of urea act as nitrogen source and in-situ reaction results in doping of graphitic nanotubes with nitrogen species, which is highly beneficial for electrochemical properties of resultant material, NGTs (Cao et al., 2012). The formation of NGTs is confirmed by XRD analysis, which shows two peaks at 2θ equals to 23.61° (0 0 2), and 43.69° (1 0 1). The interlayer spacing of these peaks were found to be 0.325 and 0.334 nm, respectively. These peaks are in good agreement with XRD peaks of graphitic carbon and their intensities confirmed the crystallinity of synthesized NGTs as shown in Fig. 1**b**. No peak was traced for N element, which is attributed to its low content (Zhang et al., 2018b). Fig. 1**c** shows the nitrogen adsorption and desorption isotherms of NGTs. The BET specific surface area of NGTs was found to be around 35.21 $m^2$ $g^{-1}$, which is sufficient for storage of guest ions (Chaikittisilp et al., 2014; Lü et al., 2015; Rashad et al., 2015). Careful observation revealed that synthesized NGTs

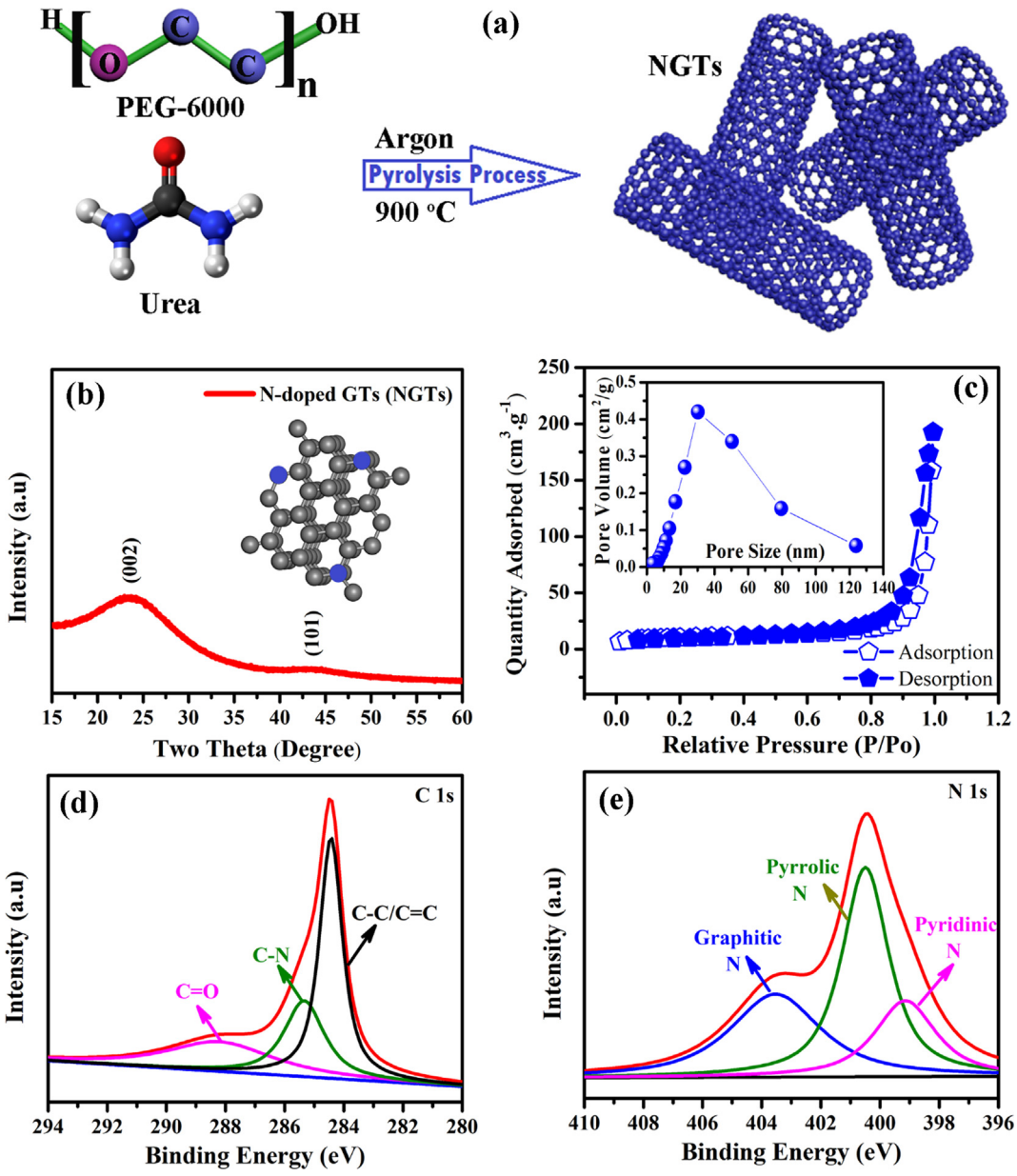


**Fig. 1** (a) Sketch diagram showing the synthesis of nitrogen-doped graphitic nanotubes, (b) X-ray diffraction, (c) Brunauer-Emmett-Teller results with pore size distribution (inset), high-resolution XPS spectra of C 1s (d), and N 1s (e).

are mesoporous as confirmed by IV traits of adsorption and desorption of nitrogen isotherms (Fig. 1**c**). The presence of nitrogen inside the graphitic tubes was confirmed by XPS technique as shown in **Figure S1 (a)**, which confirmed the presence of N doping inside GTs. Fig. 1**d** shows the XPS spectrum of C 1 s, where peaks with binding energies equal to 284.45, 285.33, and 288.25 e V corresponds to C – C/C = C, C – N, and C = O bonds, respectively. The XPS spectrum of N 1 s is shown in Fig. 1**e**, where peaks with binding energies equal to 399.13, 400.52, and 403.50 e V corresponds to pyridinic N, pyrrolic N, and graphitic N, respectively (Jian et al., 2015; Asif et al., 2018; Xiong et al., 2018). The presence of N 1 s peaks confirmed the doping of nitrogen inside the graphitic nanotubes. Raman spectra of NGTs is shown in Figure S1 (b). It can be seen that Raman spectra consist of D-band and G-band. D-band corresponds to disorders present inside the carbon materials owing to structural defects, whereas G-band is associated with planer stretching motion between $sp^2$-hybridized atoms. D-band and G-band were observed at about 1326, and 1570 $cm^{-1}$, respectively. Broader D-bands confirmed the formation of irregular shaped graphitic tubes.

The surface morphology of synthesized NGTs were examined by FESEM as shown in Fig. 2**a-c**. It can be seen that NGTs consist of aligned and uniform nanostructures with cylindrical morphology. The average length and diameters of graphitic nanotubes were found to be 1–1.5 μm and 100 nm, respectively. Careful observation revealed that no impurity or debris were observed, which confirmed the crystallinity of synthesized NGTs. Furthermore, it also proved the potential capability of adopted synthesis route. High-resolution TEM

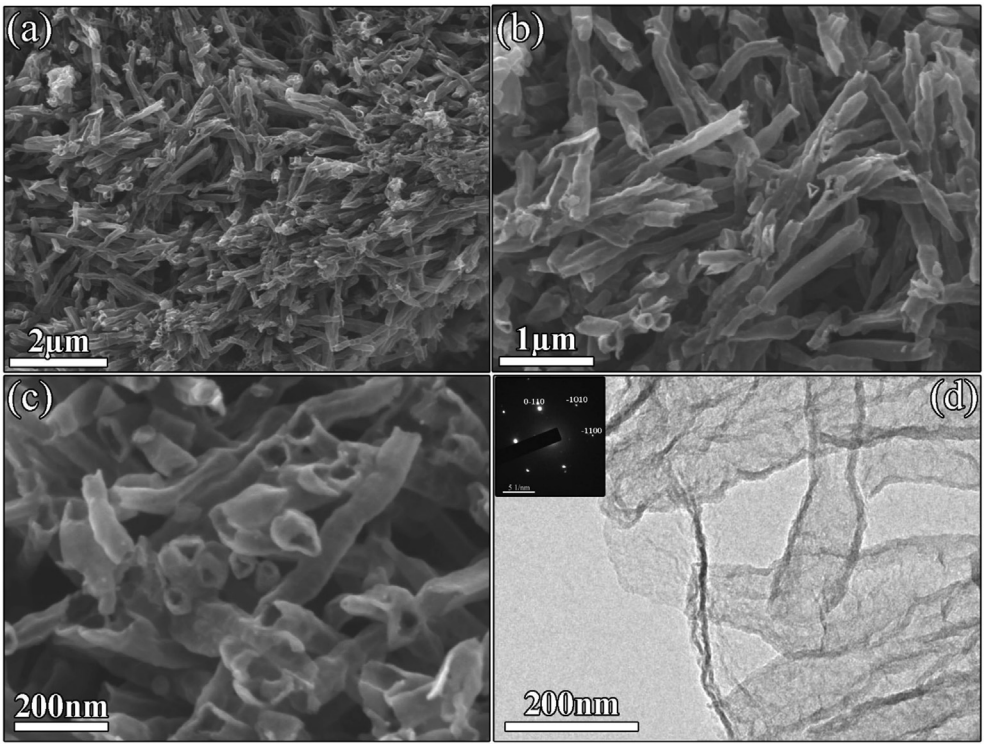


**Fig. 2** Surface morphology of NGTs: Low and high magnification FESEM (a-c) and TEM (d) images displaying the formation of tubular nanostructures with average diameter of 100 nm and SAED pattern shown in the inset of (d).

image (Fig. 2**d**) was taken to examine the number of graphitic layers. TEM image confirmed that tube wall consist of 4–7 graphitic layers. The SAED pattern revealed the high purity and crystallinity of synthesized NGTs. Synthesized material with tubular structure is highly efficient to transport and store the large atomic size guest ions during charging and discharging processes (Zhu et al., 2019).

Synthesized NGTs material was tested as positive electrode against potassium metal anode using half-cells. The CV tests were carried out between 0.9 and 3.3 V at different scan rates (0.1–2.0 mV $s^{-1}$). Fig. 3**a** shows the CV profiles of NGTs at a fixed scan rate. It can be seen that solid electrolyte interface (SEI) layer was formed as confirmed by first abnormal CV curve. During subsequent cycles, the shape of curves slightly changes and a clear redox peak was observed at 1.3 V (which confirms the insertion of guest ions inside nanotubes and is consistent with charge discharge curves), however its intensity was very low. When CV was measured at different scan rates (0.1–2.0 mV $s^{-1}$), the peak position was shifted towards the higher voltage as shown in Fig. 3**b**. Furthermore, the peak currents were also increased with increase in scan rate, which is in good agreement with Lindström's relation ($\boldsymbol{i = a.\ v^{\,b}}$) (Lindström et al., 1997). Where factor $\boldsymbol{b}$ represents the nature of reaction and is equal to slop of $\boldsymbol{\log (i) - \log (v)}$ plots. If the value of $\boldsymbol{b}$ is 0.5, then the reaction is diffusion-controlled and if it is equal to 1.0, then reaction is surface controlled. The values of $\boldsymbol{b}$ were estimated to be 0.6932 (anodic) and 0.7856 (cathodic), which confirmed that storage of $K^+$ inside NGTs cathode is surface-controlled (**Figure S1 (c)**). The ratio of surface and diffusion controlled chemical reaction can be quantified using following relation (Wang et al., 2007; Augustyn et al., 2013).

$$i(V) = k_1 v + k_2 v^{1/2} \tag{1}$$

Where, $\boldsymbol{k_1}$ and $\boldsymbol{k_2}$ are constants. The factor $\boldsymbol{k_1 v}$ represents the capacitive or surface contribution and factor $\boldsymbol{k_2 v^{1/2}}$ represents the diffusion-controlled process. Both constants ($\boldsymbol{k_1}$ and $\boldsymbol{k_2}$) were calculated and capacitive and diffusion contributions are quantified using above equation as shown in Fig. 3**c**. It can be seen that increase in scan rate, increases the capacitive currents. For example, the capacitive contribution was increased from 20.1 to 55.6%, when scan rate was increased from 0.1 to 2.0 mV $s^{-1}$. Similarly, when the half-cell was cycled at the scan rate of 0.5 mV $s^{-1}$, 35.9% of the total current was surface controlled as shown in Fig. 3**d**. The increase in surface controlled reaction is highly beneficial for structural stability of cathodes.

Fig. 4**a** shows the rate capability of NGTs cathode, where current densities were varied from 20 to 1000, and then back to 20 mA $g^{-1}$. The first cycle exhibited the specific capacity of about 350 mA $g^{-1}$ with coulombic efficiency of about 88%. Experimental result revealed the specific capacities of 220, 105, 62, 48, 35, and 15 mA h $g^{-1}$ at the current densities of 20, 40, 100, 200, 400, and 1000 mA $g^{-1}$, respectively. When current density was recovered back to its original value (20 mA $g^{-1}$), the specific capacity of 212 mA h $g^{-1}$ was retained, which confirmed the high rate performance of synthesized NGTs. As shown in Fig. 4**b,** the charge–discharge curves at different current densities revealed the absence of voltage platforms, which is consistent with cyclic voltammetry results. Table 1 shows the comparison of present work with previously reported Prussian blue analogous, different carbons, metal phosphates, metal oxides, and metal sulfides for PIBs. Compared with literature reports, the NGTs electrode exhibited

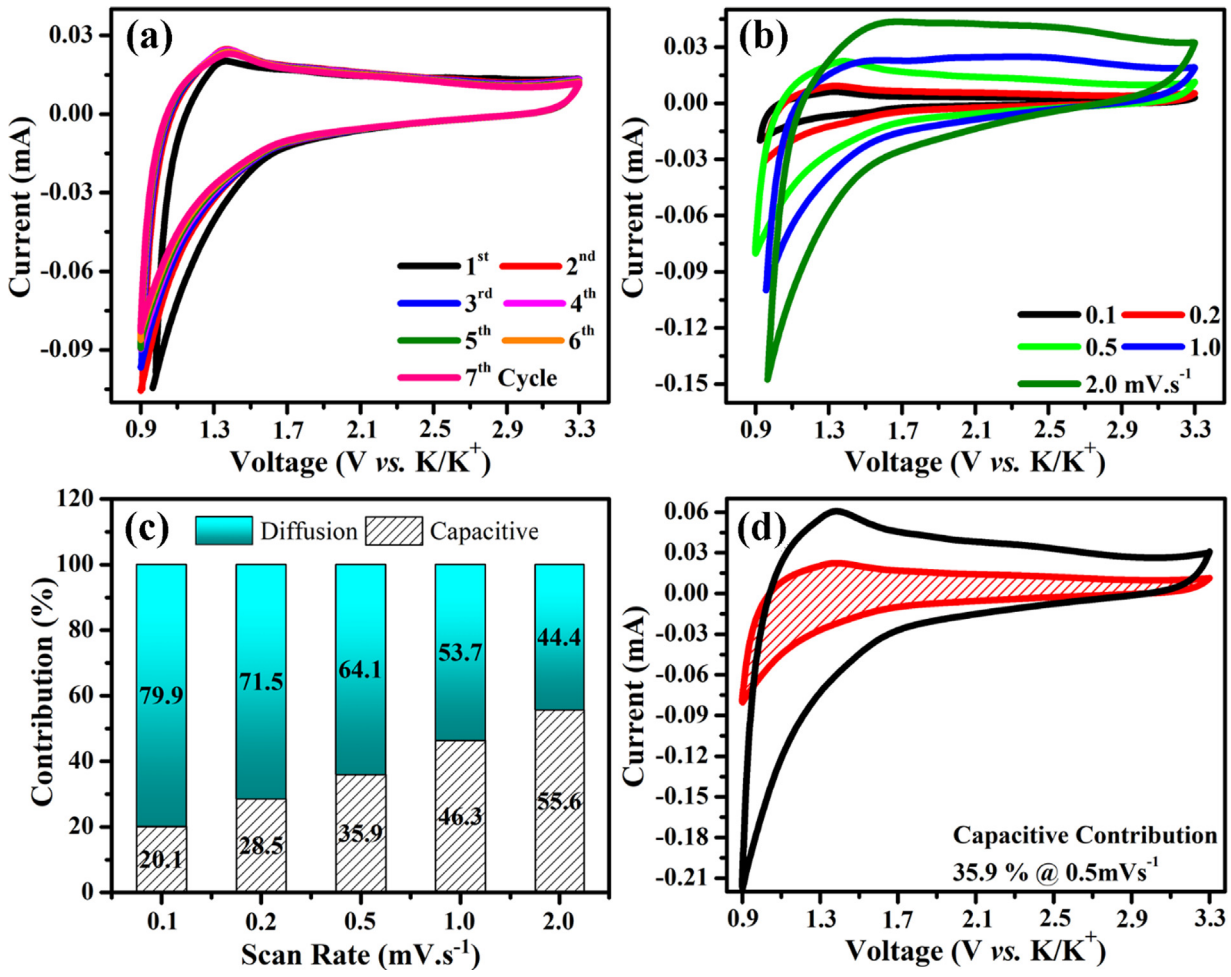


**Fig. 3** Cyclic voltammetry results of NGTs (a) CV profiles (1 − 7th Cycles) at 0.5 mV $s^{-1}$, (b) CV profiles at different scan rates (0.1–2.0 mV $s^{-1}$), (c) capacitive and diffusion contributions at different scan rates and (d) CV profiles with shaded area representing the capacitive contribution at 0.5 mV $s^{-1}$.

much better specific capacity and working voltage, thus can be considered as a new kind of electrode materials for post-lithium batteries. The excellent electrochemical properties of NGTs-based PIBs were attributed to the mesoscopic nanostructure with tubular morphology of NGTs, more nitrogen based active sites (i.e. graphitic nitrogen, pyrrolic nitrogen) which are highly beneficial to accommodate the storage and transportation of large atomic size guest ions (Zhu et al., 2019).

Fig. 4**c** shows the cycle stability of NGTs electrode up to 200 cycles at the current density of 100 mA $g^{-1}$. It can be seen that reversible capacity decayed sharply in first few cycles and then it became normal. This sharp decay was attributed to the deposition of undissolved $KPF_6$ salt sediments from the electrolyte solution as shown in **Figure S2.** The specific capacity of 81.2 mA h $g^{-1}$ was retained after 200 cycles, showing the significant capacity retentions. The improved capacity retention was attributed to the crystalline and conductive nature of NGTs network, which supports the surface controlled process during redox reactions (Song et al., 2018). To examine the bulk resistance and interfacial kinetics of NGTs-based PIBs, the electrochemical impedance spectroscopy (EIS) test was conducted between 0.01–$10^6$ Hz and data was refined using Z-view software as shown in Fig. 5**a and S4.** The corresponding equivalent circuit of Nyquist plot is shown in **Figure S3.** Nyquist plot shows the presence of a semicircle (corresponding to the charge transfer resistance, $R_{ct}$: 603.34 Ω) and a slop line (corresponding to the Warburg factor, $\sigma$). The relation between diffusion coefficient ($D$) and Warburg factor ($\sigma$) is given in Eq. (2) (Yin et al., 2003).

$$D = R^2T^2/2A^2n^4F^4C^2\sigma^2 \quad (2)$$

Where $R$ is gas constant, $T$ is absolute temperature, $A$ is the surface area of the positive electrode, $n$ is number of electrons per molecule; $F$ is Faraday constant, $C$ is concentration of potassium-ions, and $\sigma$ is Warburg factor. The relation between Warburg factor $\sigma$ and $Z'$ as given in Eq. (3) (Cheng et al., 2015).

$$Z' = R_s + R_{ct} + \sigma\omega^{-1/2} \quad (3)$$

Where, $R_s$ is resistance between electrode and electrolyte, $R_{ct}$ is charge transfer resistance, and $\omega$ is angular frequency. The relationship between $Z'$ and $\omega^{-1/2}$ is shown in Fig. 5**b**, and slope of fitting line symbolizes the $\sigma$. Using Eqs. (2) and (3), the diffusion coefficient of $K^+$ ion in NGTs network was calculated to be 3.8853 × $10^{-13}$ $cm^2$ $s^{-1}$ (Liu et al., 2018a; Liu et al., 2018c).

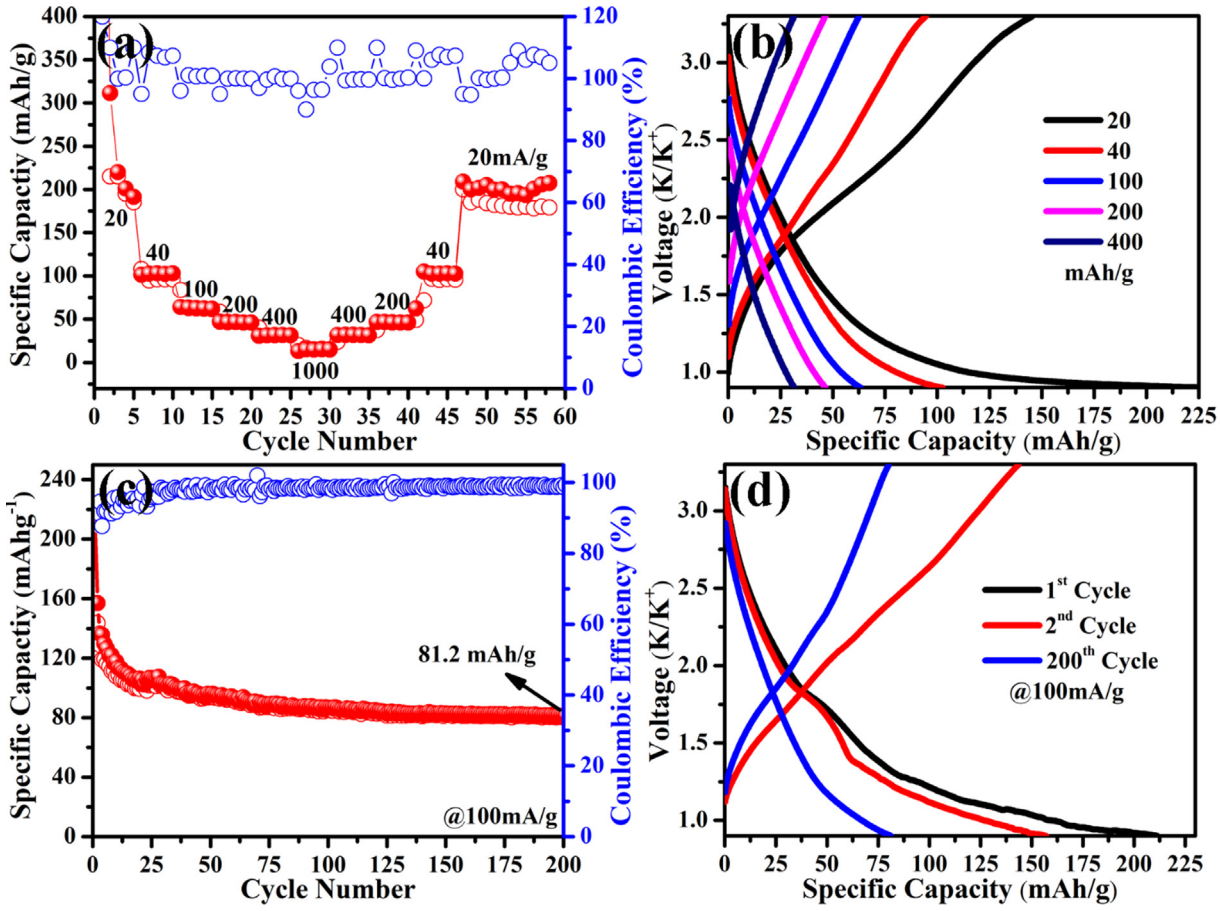


**Fig. 4** (a) Rate performance, (b) Galvanostatic charging/discharging profiles at current densities of 20, 40, 100, 200, 400, 1000 mA h $g^{-1}$, (c) Cycle stability, and (d) 1st, 2nd and 200th charging/discharging profiles (at 100 mA h $g^{-1}$) of NGTs-based half-cells (solid spheres: discharge capacity and empty circles: charge capacity).

**Table 1** Comparison of present work (NGTs) with literature reports on PIBs.

| Materials | Specific capacity (mA h $g^{-1}$) | Current density (mA $g^{-1}$) | References |
|---|---|---|---|
| Graphitic Carbons | 98 | 200 | (Cohn et al., 2016) |
| $K_2Ti_8O_{17}$ | 120 | 20 | (Han et al., 2016b) |
| $K_2Ti_4O_9$ | 95 | 30 | (Kishore et al., 2016) |
| $KTi_2(PO_4)_3/C$ | 85 | 64 | (Han et al., 2016a) |
| $Fe^{III}Fe^{III}(CN)_6$ | 140 | 111 | (Padigi et al., 2015) |
| $Co_3O_4$-$Fe_2O_3/C$ | 100 | 50 | (Sultana et al., 2017) |
| $FeFe(CN)_6$ | 120 | 125 | (Shadike et al., 2017) |
| $FePO_4$ | 140 | 10 | (Mathew et al., 2014) |
| $K_2FeO_4$ | 105 | 0.05 | (Do et al., 2013) |
| $K_{0.7}Fe_{0.5}Mn_{0.5}O_2$ | 118 | 100 | (Wang et al., 2017) |
| $MoS_2$ | 65 | 20 | (Ren et al., 2017) |
| $K_{0.6}Ni_{1.2}Fe(CN)_6$ 3·.$6H_2O$ | 60 | 45 | (Wessells et al., 2011) |
| NCNFs | 245 | 50 | (Xu et al., 2018) |
| NBCNTs | 310 | 100 | (Liu et al., 2018b) |
| NCNTs | 280 | 20 | (Xiong et al., 2018) |
| **NGTs** | **220** | **20** | **Present Work** |

## 4. Conclusions

One-step solid-state reaction method was employed for in-situ synthesis of nitrogen-doped graphitic nanotubes (NGTs). The material characterizations such as SEM and TEM revealed the uniform, tubular and mesoscopic structure of synthesized NGTs. The doping of nitrogen species was confirmed by XPS analysis. The synthesized NGTs network provides numer-

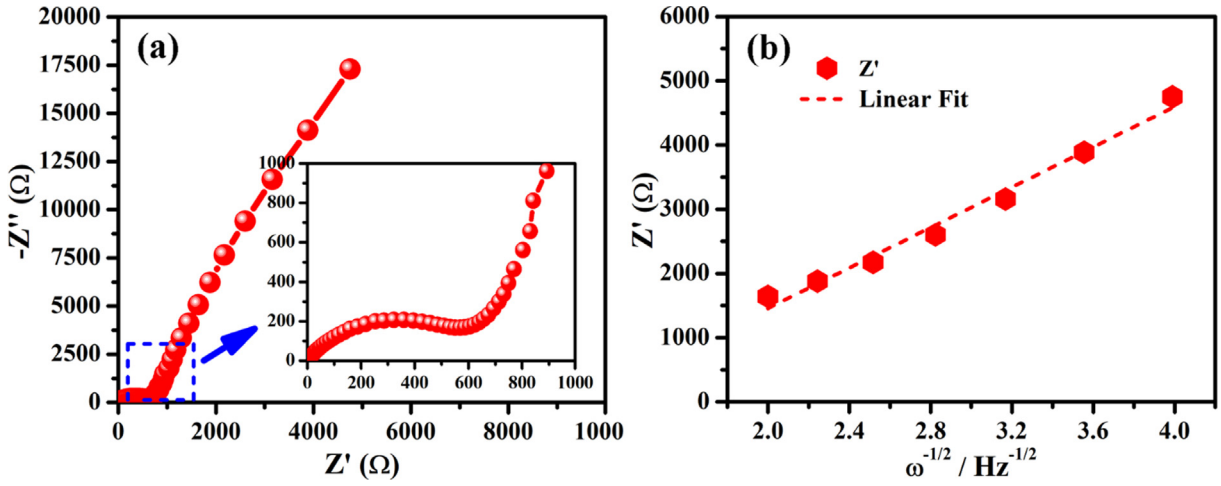


**Fig. 5** (a) Nyquist plot (inset showing magnified area), and (b) Plot between Z' and $\omega^{-1/2}$ in low frequency region.

ous reaction sites (i.e. $N_p$ and $N_g$) and fast electron/$K^+$ transportation during redox reactions. The NGTs was employed as electrode material against potassium metal anode in the presence of carbonate based electrolytes. Electrochemical results revealed the excellent rate capability (220 mA h $g^{-1}$/20 mA $g^{-1}$) and cycle life (81.2 mA h $g^{-1}$ is maintained even after 200 cycles). In addition, electrochemical processes were quantitatively analyzed using theoretical models to elaborate the diffusion controlled and surface-controlled contributions. The $K^+$ ion diffusion coefficient inside the NGTs network was also quantified to correlate the electrochemical properties. We hope this effort will open new horizons on the rational design of carbon networks for rechargeable metal ion batteries.

## Declaration of Competing Interest

None.

## Acknowledgements

This research was supported by JUST Research Start-Up Fund (1062921905).

## Appendix A. Supplementary material

Supplementary data to this article can be found online at https://doi.org/10.1016/j.arabjc.2021.103113.

## References

Asif, M., Rashad, M., Ali, Z., Qiu, H., Li, W., Pan, L., Hou, Y., 2018. Ni-doped MnO2/CNT nanoarchitectures as a cathode material for ultra-long life magnesium/lithium hybrid ion batteries. Mater. Today Energy 10, 108–117.

Augustyn, V., Come, J., Lowe, M.A., Kim, J.W., Taberna, P.-L., Tolbert, S.H., Abruña, H.D., Simon, P., Dunn, B., 2013. High-rate electrochemical energy storage through Li+ intercalation pseudocapacitance. Nat. Mater. 12, 518.

Cao, L., Li, Z., Fan, G., Jiang, L., Zhang, D., Moon, W.-J., Kim, Y.-S., 2012. The growth of carbon nanotubes in aluminum powders by the catalytic pyrolysis of polyethylene glycol. Carbon 50, 1057–1062.

Cao, W., Zhang, E., Wang, J., Liu, Z., Ge, J., Yu, X., Yang, H., Lu, B., 2019. Potato derived biomass porous carbon as anode for potassium ion batteries. Electrochim. Acta 293, 364–370.

Chaikittisilp, W., Torad, N.L., Li, C., Imura, M., Suzuki, N., Ishihara, S., Ariga, K., Yamauchi, Y., 2014. Synthesis of Nanoporous Carbon–Cobalt-Oxide Hybrid Electrocatalysts by Thermal Conversion of Metal-Organic Frameworks. Chem. – A Eur. J. 20, 4217–4221.

Chen, L., Zhao, Y., 2019. Exploration of p-Na2C6H2O6-based organic electrode materials for sodium-ion and potassium-ion batteries. Mater. Lett. 243, 69–72.

Cheng, Y., Feng, K., Zhou, W., Zhang, H., Li, X., Zhang, H., 2015. A Bi-doped Li3V2(PO4)3/C cathode material with an enhanced high-rate capacity and long cycle stability for lithium ion batteries. Dalton Trans. 44, 17579–17586.

Cohn, A.P., Muralidharan, N., Carter, R., Share, K., Oakes, L., Pint, C.L., 2016. Durable potassium ion battery electrodes from high-rate cointercalation into graphitic carbons. J. Mater. Chem. A 4, 14954–14959.

Daigle, J.-C., Asakawa, Y., Beaupré, M., Arnold, A.A., Laul, D., Trudeau, M., Zaghib, K., 2019. A versatile method for grafting polymers onto Li4Ti5O12 particles applicable to lithium-ion batteries. J. Power Sources 421, 116–123.

Do, G.X., Paul, B.J., Mathew, V., Kim, J., 2013. Nanostructured iron ((iii) oxyhydroxide/(vi) oxide) composite as a reversible Li, Na and K-ion insertion electrode for energy storage devices. J. Mater. Chem. A 1, 7185–7190.

Fagerlund, G., 1973. Determination of specific surface by the BET method. Matériaux et Construction 6, 239–245.

Gong, X., Liu, G., Li, Y., Yu, D.Y.W., Teoh, W.Y., 2016. Functionalized-Graphene Composites: Fabrication and Applications in Sustainable Energy and Environment. Chem. Mater. 28, 8082–8118.

Han, J., Niu, Y., Bao, S.-J., Yu, Y.-N., Lu, S.-Y., Xu, M., 2016a. Nanocubic KTi2(PO4)3 electrodes for potassium-ion batteries. Chem. Commun. 52, 11661–11664.

Han, J., Xu, M., Niu, Y., Li, G.-N., Wang, M., Zhang, Y., Jia, M., Li, C.M., 2016b. Exploration of K2Ti8O17 as an anode material for potassium-ion batteries. Chem. Commun. 52, 11274–11276.

Ji, D., Peng, S., Safanama, D., Yu, H., Li, L., Yang, G., Qin, X., Srinivasan, M., Adams, S., Ramakrishna, S., 2017. Design of 3-Dimensional Hierarchical Architectures of Carbon and Highly Active Transition Metals (Fe Co, Ni) as Bifunctional Oxygen Catalysts for Hybrid Lithium-Air Batteries. Chem. Mater. 29, 1665–1675.

Jian, Z., Luo, W., Ji, X., 2015. Carbon Electrodes for K-Ion Batteries. J. Am. Chem. Soc. 137, 11566–11569.

Kim, H., Kim, J.C., Bianchini, M., Seo, D.-H., Rodriguez-Garcia, J., Ceder, G., 2018. Recent Progress and Perspective in Electrode Materials for K-Ion Batteries. Adv. Energy Mater. 8, 1702384.

Kishore, B., G, V., Munichandraiah, N., 2016. K2Ti4O9: A Promising Anode Material for Potassium Ion Batteries. J. Electrochem. Soc., 163, A2551-A2554.

Li, Y., Sun, Y., Xu, G., Lu, Y., Zhang, S., Xue, L., Jur, J.S., Zhang, X., 2014. Tuning electrochemical performance of Si-based anodes for lithium-ion batteries by employing atomic layer deposition alumina coating. J. Mater. Chem. A 2, 11417–11425.

Lindström, H., Södergren, S., Solbrand, A., Rensmo, H., Hjelm, J., Hagfeldt, A., Lindquist, S.-E., 1997. Li+ Ion Insertion in TiO2 (Anatase). 2. Voltammetry on Nanoporous Films. J. Phys. Chem. B 101, 7717–7722.

Liu, X., Gao, S., Yang, P., Wang, B., Ou, J.Z., Liu, Z., Wang, Y., 2018a. Synergetic coupling of Pd nanoparticles and amorphous MoSx toward highly efficient electrocatalytic hydrogen evolution reactions. Appl. Mater. Today 13, 158–165.

Liu, Y., Yang, C., Pan, Q., Li, Y., Wang, G., Ou, X., Zheng, F., Xiong, X., Liu, M., Zhang, Q., 2018b. Nitrogen-doped bamboo-like carbon nanotubes as anode material for high performance potassium ion batteries. J. Mater. Chem. A 6, 15162–15169.

Liu, Z., Zhang, X., Wang, B., Xia, M., Gao, S., Liu, X., Zavabeti, A., Ou, J.Z., Kalantar-Zadeh, K., Wang, Y., 2018c. Amorphous MoSx-Coated TiO2 Nanotube Arrays for Enhanced Electrocatalytic Hydrogen Evolution Reaction. J. Phys. Chem. C 122, 12589–12597.

Lü, Y., Wang, Y., Li, H., Lin, Y., Jiang, Z., Xie, Z., Kuang, Q., Zheng, L., 2015. MOF-Derived Porous Co/C Nanocomposites with Excellent Electromagnetic Wave Absorption Properties. ACS Appl. Mater. Interfaces 7, 13604–13611.

Luo, W., Wan, J., Ozdemir, B., Bao, W., Chen, Y., Dai, J., Lin, H., Xu, Y., Gu, F., Barone, V., Hu, L., 2015. Potassium Ion Batteries with Graphitic Materials. NANO Lett. 15, 7671–7677.

Mathew, V., Kim, S., Kang, J., Gim, J., Song, J., Baboo, J.P., Park, W., Ahn, D., Han, J., Gu, L., Wang, Y., Hu, Y.-S., Sun, Y.-K., Kim, J., 2014. Amorphous iron phosphate: potential host for various charge carrier ions. Npg Asia Mater. 6, e138.

Obrovac, M.N., Chevrier, V.L., 2014. Alloy Negative Electrodes for Li-Ion Batteries. Chem. Rev. 114, 11444–11502.

Padigi, P., Thiebes, J., Swan, M., Goncher, G., Evans, D., Solanki, R., 2015. Prussian Green: A High Rate Capacity Cathode for Potassium Ion Batteries. Electrochim. Acta 166, 32–39.

Rashad, M., Pan, F., Yu, Z., Asif, M., Lin, H., Pan, R., 2015. Investigation on microstructural, mechanical and electrochemical properties of aluminum composites reinforced with graphene nanoplatelets. Prog. Nat. Sci.: Mater. Int. 25, 460–470.

Ren, X., Zhao, Q., McCulloch, W.D., Wu, Y., 2017. MoS2 as a long-life host material for potassium ion intercalation. NANO Res. 10, 1313–1321.

Shadike, Z., Shi, D.-R., Tian, W., Cao, M.-H., Yang, S.-F., Chen, J., Fu, Z.-W., 2017. Long life and high-rate Berlin green FeFe(CN)6 cathode material for a non-aqueous potassium-ion battery. J. Mater. Chem. A 5, 6393–6398.

Shannon, R.D., 1976. Revised Effective Ionic Radii and Systematic Studies of Interatomie Distances in Halides and Chaleogenides. Acta Crystallogr. A32, 751–767.

Share, K., Cohn, A.P., Carter, R., Rogers, B., Pint, C.L., 2016. Role of Nitrogen-Doped Graphene for Improved High-Capacity Potassium Ion Battery Anodes. ACS Nano 10, 9738–9744.

Singh, N., Arthur, T.S., Ling, C., Matsui, M., Mizuno, F., 2013. A high energy-density tin anode for rechargeable magnesium-ion batteries. Chem. Commun. 49, 149–151.

Song, J., Lv, X., Jiao, Y., Wang, P., Xu, M., Li, T., Chen, X., Li, J., Zhang, Z., 2018. Catalyst nanoarchitecturing via functionally implanted cobalt nanoparticles in nitrogen doped carbon host for aprotic lithium-oxygen batteries. J. Power Sources 394, 122–130.

Sultana, I., Rahman, M.M., Mateti, S., Ahmadabadi, V.G., Glushenkov, A.M., Chen, Y., 2017. K-ion and Na-ion storage performances of Co3O4–Fe2O3 nanoparticle-decorated super P carbon black prepared by a ball milling process. Nanoscale 9, 3646–3654.

Suo, G., Li, D., Feng, L., Hou, X., Yang, Y., Wang, W., 2019. SnO2 nanosheets grown on stainless steel mesh as a binder free anode for potassium ion batteries. J. Electroanal. Chem. 833, 113–118.

Tao, M., Du, G., Zhang, Y., Gao, W., Liu, D., Luo, Y., Jiang, J., Bao, S., Xu, M., 2019. TiOxNy nanoparticles/C composites derived from MXene as anode material for potassium-ion batteries. Chem. Eng. J. 369, 828–833.

Vishnuprakash, P., Nithya, C., Premalatha, M., 2019. Exploration of V2O5 nanorod@rGO heterostructure as potential cathode material for potassium-ion batteries. Electrochim. Acta 309, 234–241.

Wang, J., Polleux, J., Lim, J., Dunn, B., 2007. Pseudocapacitive Contributions to Electrochemical Energy Storage in TiO2 (Anatase) Nanoparticles. J. Phys. Chem. C 111, 14925–14931.

Wang, W., Liu, L., Wang, P.-F., Zuo, T.-T., Yin, Y.-X., Wu, N., Zhou, J.-M., Wei, Y., Guo, Y.-G., 2018. A novel bismuth-based anode material with a stable alloying process by the space confinement of an in situ conversion reaction for a rechargeable magnesium ion battery. Chem. Commun. 54, 1714–1717.

Wang, X., Xu, X., Niu, C., Meng, J., Huang, M., Liu, X., Liu, Z., Mai, L., 2017. Earth Abundant Fe/Mn-Based Layered Oxide Interconnected Nanowires for Advanced K-Ion Full Batteries. NANO Lett. 17, 544–550.

Wessells, C.D., Peddada, S.V., Huggins, R.A., Cui, Y., 2011. Nickel Hexacyanoferrate Nanoparticle Electrodes For Aqueous Sodium and Potassium Ion Batteries. NANO Lett. 11, 5421–5425.

Xiong, P., Zhao, X., Xu, Y., 2018. Nitrogen-Doped Carbon Nanotubes Derived from Metal-Organic Frameworks for Potassium-Ion Battery Anodes. ChemSusChem 11, 202–208.

Xu, Y., Zhang, C., Zhou, M., Fu, Q., Zhao, C., Wu, M., Lei, Y., 2018. Highly nitrogen doped carbon nanofibers with superior rate capability and cyclability for potassium ion batteries. Nat. Commun. 9, 1720.

Xue, L., Li, Y., Gao, H., Zhou, W., Lü, X., Kaveevivitchai, W., Manthiram, A., Goodenough, J.B., 2017. Low-Cost High-Energy Potassium Cathode. J. Am. Chem. Soc. 139, 2164–2167.

Yang, Q., Wang, Z., Xi, W., He, G., 2019. Tailoring nanoporous structures of Ge anodes for stable potassium-ion batteries. Electrochem. Commun. 101, 68–72.

Yin, S.C., Grondey, H., Strobel, P., Anne, M., Nazar, L.F., 2003. Electrochemical Property: Structure Relationships in Monoclinic Li3-yV2(PO4)3. J. Am. Chem. Soc. 125, 10402–10411.

Zhang, H., Wang, L., Li, Q., Ma, L., Wu, T., Ma, Y., Wang, J., Du, C., Yin, G., Zuo, P., 2018a. Cobalt nanoparticle-encapsulated carbon nanowire arrays: Enabling the fast redox reaction kinetics of lithium-sulfur batteries. Carbon 140, 385–393.

Zhang, W., Mao, J., Li, S., Chen, Z., Guo, Z., 2017. Phosphorus-Based Alloy Materials for Advanced Potassium-Ion Battery Anode. J. Am. Chem. Soc. 139, 3316–3319.

Zhang, W., Mao, S., Xu, J., Xu, Q., Zhang, M., Zhou, J., Song, L., Guan, R., Yue, L., 2018b. Fabrication of three-dimensional hollow C@CoO@graphene composite anode for long-life Li-ion batteries. Electrochim. Acta 291, 206–215.

Zhu, C., Ma, Y., Zang, W., Guan, C., Liu, X., Pennycook, S.J., Wang, J., Huang, W., 2019. Conformal dispersed cobalt nanoparticles in hollow carbon nanotube arrays for flexible Zn-air and Al-air batteries. Chem. Eng. J. 369, 988–995.